

¹ The imbricated foreshock and aftershock activities of
² the Balsorano (Italy) M_w 4.4 normal fault earthquake
³ and implications for earthquake initiation

⁴ H. S. Sánchez-Reyes¹, D. Essing¹, E. Beaucé², P. Poli¹¹

⁵ *¹Institute of Earth Sciences, University Grenoble Alpes, Grenoble 38100, France*

⁶ *²Department of Earth, Atmospheric, and Planetary Sciences, Massachusetts Institute of
7 Technology, Cambridge, MA, United States*

⁸ **Corresponding author: hugo.sanchez-reyes@univ-grenoble-alpes.fr*

⁹ **Key words:**

¹⁰ • earthquake initiation process

¹¹ • earthquake sequence

¹² • spatio-temporal evolution

¹³ **Key points:**

¹⁴ • The analysis of the 2019 Balsorano earthquake sequence reveals that imbricated com-
¹⁵ plex processes occur before and after the main earthquake

¹⁶ • Clear differences between foreshocks and aftershocks are highlighted by the distinct
¹⁷ spatio-temporal patterns unraveled by our analysis

¹⁸ • These results demonstrate that simple earthquake preparation models are not suitable
¹⁹ enough to correctly mimic the observed complex reality

Abstract

21 Foreshocks in the form of microseismicity are among the most powerful tools to
22 study the physical processes that occur before main earthquakes. However, their
23 detection and precise characterization is still sparse, especially for small to moderate-
24 sized earthquakes ($M_w < 6$). We present here a detailed foreshock analysis for the
25 November 7, 2019, Balsorano (Italy) normal fault earthquake ($M_w 4.4$). To improve
26 the detection of the microseismicity before and after the mainshock, we use six three-
27 component broadband receivers at distances of less than 75 km from the targeted
28 seismicity, through template matching. To improve the understanding of the physical
29 mechanism(s) behind the earthquake initiation process, as well as other accompanying
30 phenomena, we also detail the spatio-temporal evolution of the sequence associated
31 to this medium-sized earthquake, using waveform clustering and hypocenter
32 relocation. Clear differences between foreshocks and aftershocks are revealed by this
33 analysis. Moreover, five distinct spatio-temporal patterns associated to the different
34 seismic activities are revealed. The observed spatio-temporal behavior shown by
35 the foreshocks highlights a complex initiation process, which apparently starts on
36 an adjacent unmapped antithetic fault. Finally, the aftershock activity comprises
37 four different clusters with distinct spatio-temporal patterns, which suggests that the
38 different clusters in this sequence have distinct triggering mechanisms.

Introduction

40 The detection of signals that can inform us about a forthcoming earthquake is fundamental
41 to build physical models that mimic the processes behind the triggering and nucleation of
42 earthquakes. These physical models are important because they provide us the basis to
43 characterize earthquakes. Therefore, the study and analysis of precursory signals are of
44 great importance. Over the last 25 years, numerous studies have reported a wide range of
45 observations that appear to be connected with the physics that precedes large seismic events

⁴⁶ (*e.g.* Rikitake, 1975; Jones and Molnar, 1979; Molchanov et al., 1998; Eftaxias et al., 2000;
⁴⁷ Virk and Walia, 2001; Singh et al., 2010; De Santis et al., 2019; Jones, 1985; Abercrombie
⁴⁸ and Mori, 1996; Felzer et al., 2004; Dodge et al., 1996; Ellsworth and Bulut, 2018; Yoon
⁴⁹ et al., 2019; Reasenberg, 1999; Ruiz et al., 2017, 2014a). Among these, some of the most
⁵⁰ compelling are the ones based on seismological characterization of foreshock sequences,
⁵¹ as well as other seismological observations and their relationships with mainshocks (*e.g.*
⁵² Jones, 1985; Abercrombie and Mori, 1996; Reasenberg, 1999; Felzer et al., 2004; Dodge
⁵³ et al., 1996; Bouchon et al., 2011; Ruiz et al., 2014b, 2017; Ellsworth and Bulut, 2018; Yoon
⁵⁴ et al., 2019). Foreshocks are thus one of the most useful tools to understand the physics of
⁵⁵ earthquake initiation in real faults (Brune, 1979; Abercrombie and Mori, 1996; Malin et al.,
⁵⁶ 2018). Therefore, it is important to improve foreshock observations and characterization,
⁵⁷ particularly for the more frequent small to moderate-sized events (*i.e.* $M_w < 6$), as these
⁵⁸ might share similar physical processes with larger events. These improved observations
⁵⁹ may shed light on the physical processes that occur during the triggering and nucleation of
⁶⁰ earthquakes and will drive future research that focuses on theoretical and numerical models
⁶¹ to better characterize earthquake occurrence in real and complex faults.

⁶² Earthquake initiation (*e.g.* Kato et al., 2012; Schurr et al., 2014; Tramutoli et al., 2015)
⁶³ and earthquake nucleation/triggering (*e.g.* Dieterich, 1992; Ellsworth and Beroza, 1995;
⁶⁴ Rubin and Ampuero, 2005) are two different, and perhaps overlapping, phases of the seis-
⁶⁵ mic cycle. While the first is understood to occur over the longer term preceding a large
⁶⁶ event (*i.e.*, days or months, to years), the second occurs some minutes toThe results of
⁶⁷ the spatio-temporal evolution for the identified clusters suggest complex evolution of the
⁶⁸ seismicity. Two fault planes are activated during the sequence, with foreshocks primarily
⁶⁹ occurring on the antithetic fault plane (Fig. 5a, cross-section), similarly to part of the
⁷⁰ foreshock activity that was observed for the L'Aquila normal fault earthquake (Chiaraluce
⁷¹ et al., 2011). Relying only on our observations, it is hard to unravel which mechanism(s)
⁷² might be responsible for the occurrence of the foreshocks, and thus the driving of the

main event. For example, there are no exponential or power-law increments of events seen while approaching the main event (Papazachos, 1975; Kagan and Knopoff, 1978), which might suggest accelerating aseismic slip (Dodge et al., 1996; Bouchon et al., 2011; Tape et al., 2018). Neither are any spatial patterns seen (*e.g.*, migrations) that might suggest the same mechanism, or might alternatively indicate triggering by stress transfer (Dodge et al., 1996; Ellsworth and Bulut, 2018; Yoon et al., 2019). However, we clearly outline the differences between the foreshocks and aftershocks. In particular, the foreshocks occur in a more temporal clustered manner, and they are closer to the hypocenter of the main event (Fig. 4a). The compact and highly temporal clustered seismicity indicates strong event interactions, and favors stress transfer as the mechanism for foreshock occurrence (COV, Schoenball and Ellsworth, 2017). seconds before the main event. Both phases, however, can be explained under the Dieterich model (1994), which relates the seismicity rate to the stressing history through a rate-and-state constitutive law. For earthquake initiation in particular for real faults, two main hypotheses are currently used to explain this process. Some authors argue that a mainshock is a consequence of a cascade process, with stress transfer in-between events, which eventually trigger the large event (*e.g.*, Dodge et al., 1996; Ellsworth and Bulut, 2018; Yoon et al., 2019). Alternatively, the initiation of an earthquake can be understood as an aseismic process that weakens the pre-existing asperities, until a larger rupture is promoted (Dodge et al., 1996; Bouchon et al., 2011; Tape et al., 2018). In the latter case, foreshocks result from the activation of brittle asperities by the surrounding slip processes. However, intermediate models that involve both triggering and aseismic slip are likely for complex faults (*e.g.* McLaskey, 2019). This complexity might result from fault heterogeneity (*e.g.*, variable stress, frictional properties) and promote imbricated sequences of foreshocks and aseismic slip (*e.g.*, Dublanchet, 2018).

The monitoring of foreshocks is today routine in laboratory experiments (Zang et al., 1998; Goebel et al., 2012; Renard et al., 2019, and references therein), while studies that focus on large earthquakes remain relatively sparse (*i.e.*, $M_w > 6$) (*e.g.*, Mogi, 1963; Aber-

100 crombie and Mori, 1996; Kato et al., 2012; Chen and Shearer, 2013; Bouchon et al., 2013;
101 Ruiz et al., 2014b). However, the recent improvements to seismological monitoring systems
102 around active faults have now provided detailed analysis of foreshocks that precede the
103 more frequent small to moderate-sized earthquakes ($M_w < 6$) (e.g., Savage et al., 2017;
104 McMahon et al., 2017; Malin et al., 2018). One intriguing feature that has emerged from
105 these more recent studies is the increased complexity (*i.e.*, fault interactions, volumetric
106 processes) that have been revealed through the availability of better data (e.g., near-fault
107 receivers) and more advanced detection methods (e.g., template matching) to study fore-
108 shocks. This complexity might challenge the actual laboratory scale and theoretical models,
109 which treat earthquake initiation as simple physical processes that occur in smooth fault
110 planes (Dieterich, 1992; Marone, 1998; Rubin and Ampuero, 2005; Liu and Rice, 2005).
111 The necessity for high-resolution characterization of foreshocks based on good data and
112 advanced data processing techniques was also suggested by a meta-analysis carried out by
113 Mignan (2014), which indicated resolution-dependent bias for earthquake initiation models
114 that were resolved using seismological data.

115 To shed new light on the physical processes that occur before relatively small earth-
116 quakes, we study here the medium-sized (M_w 4.4) Balsorano normal fault earthquake and
117 its foreshock-aftershock sequence (Fig. 1). The Italian National Institute of Geophysics and
118 Volcanology (*Istituto Nazionale di Geofisica e Vulcanologia*; INGV; [online catalog](#)) reported
119 that the main event of this sequence occurred on November 7, 2019 (17:35:21.18 UTC), ap-
120 proximately 4 km southeast of Balsorano city in central Italy (Fig. 1). The hypocenter
121 of this main event was located relatively deep in the crust (14 km), close to the transi-
122 tion zone between the upper and lower crust (10-20 km in depth), where the brittle locked
123 fault transitions into the ductile regime zone (Doglioni et al., 2011). Below this depth, the
124 lower crust is relatively seismically silent (Doglioni et al., 2011). According to a geological
125 study of the location of the main event and its focal mechanism (Supplementary Material
126 Table S1), this event ruptured the Liri fault (Roberts and Michetti, 2004), which is one of

127 the major active normal faults mapped in this region. This structure accommodates the
128 low extension rate observed in this region (*i.e.*, a few millimeters per year) (Hunstad and
129 England, 1999; Westaway, 1992; D'agostino et al., 2001; Roberts and Michetti, 2004).

130 [Figure 1]

131 In addition to the mainshock of November 7, 2019, 135 events occurred close to the
132 epicenter of the main event from October 22 to November 15, 2019 (which included 25
133 foreshocks). Starting from these cataloged events, we study here the 'anatomy' of the
134 foreshocks and aftershocks, and their relationships with the main event. With this aim,
135 continuous data from six three-component stations at less than 75 km from the mainshock
136 epicenter are used (Fig. 1; Supplementary Materials Table S2). The continuous waveforms
137 recorded are analyzed using template matching techniques (Gibbons and Ringdal, 2006;
138 Shelly et al., 2007) to detect smaller events and thus to expand upon the available seismic
139 catalog. The detected events are then relocated using the double-difference method (Wald-
140 hauser, 2001), to reveal the geometry of the main fault and to obtain new insights into
141 the fault-slip behavior(s) before and after the main seismic event. Furthermore, through
142 waveform clustering, we isolate families of earthquakes that are representative of different
143 physical processes that occur in the pre- and post-mainshock period. This combination of
144 detection, relocation, and waveform clustering reveals an imbricated seismic sequence where
145 several faults were activated, and with clear differences in the spatio-temporal properties
146 of the foreshocks and aftershocks.

147 Methods

148 **Template matching:** The analysis starts by extending the INGV seismic catalog using the
149 template matching approach (Gibbons and Ringdal, 2006). From the 135 events reported
150 by the INGV online catalog , where 25 events are identified as foreshocks, we retain only

151 the events with available P-wave and S-wave picks for all of the six stations used. We then
152 extract 4 s of signal, starting 1 s before the phase arrival time from the band-pass filtered
153 data (5-20 Hz). Using the pre-picked signals, we estimate the signal-to-noise ratio and
154 retain as templates only those events with a signal-to-noise ratio >3 at all of the stations.
155 With this data selection, 23 events are obtained (including three foreshocks) that are the
156 templates used for scanning the continuous data (Supplementary Materials Table S4). We
157 use three-component data with P waves extracted from the vertical component, and S waves
158 extracted from the East and North components.

159 In all, 28 days of continuous data are processed, from October 22 (*i.e.*, 16 days before
160 the mainshock) to November 15, 2019, using the fast matched filter algorithm from [Beaucé
et al. \(2017\)](#). The detection thresholds are set to 12 times the daily median absolute devi-
161 ation of the summed correlation coefficients over the array of stations. Finally, consecutive
162 detections with differential times of <3 s are removed (*i.e.*, the time difference between two
163 estimated origin times).

165 The final catalog contains 714 events (166 foreshocks, 547 aftershocks), which represents
166 ~ 6 -fold the number of events in the initial catalog. To estimate the magnitudes of the
167 newly detected events, we use the average root mean square in the time window containing
168 the S waves over all of the stations and components. Least-square fitting is then used
169 to obtain a linear model that relates the logarithmic of the root mean square of the 23
170 templates and their local magnitudes from the INGV catalog. This model is then used to
171 estimate the magnitude of the newly detected events. A summary of the event occurrences
172 in time together with their magnitudes is shown in Figure 2.

173 [Figure 2]

174 **Waveform-based clustering:** Clustering is widely used in seismology to recognize
175 patterns in spatio-temporal events, which include the identification of foreshock-aftershock
176 sequences and stress evolution in time (*e.g.*, [Kagan and Jackson, 1991](#); [Wehling-Benatelli](#)

177 et al., 2013; Cesca et al., 2014; Ellsworth and Bulut, 2018). Here, we apply waveform simi-
178 larity analysis (Cattaneo et al., 1999) to define groups of events that share similar locations
179 and/or a common rupture mechanism (Kagan and Jackson, 1991; Wehling-Benatelli et al.,
180 2013; Cesca et al., 2014; Ellsworth and Bulut, 2018; Cattaneo et al., 1999). For this, the
181 full normalized waveforms are used, with a 4.5-s time window (starting 0.5 s before the
182 P-wave arrival) that contains both the P phase and the S phase.

183 The waveforms of the 714 detected events recorded at the closest station to the epicenter
184 (Fig. 1, VVLD) are then correlated with each other. The correlation matrix obtained (Fig.
185 3a) is used to estimate the distance (dissimilarity) metric to perform hierarchical clustering.
186 The Ward minimum variance method is used (Ward Jr, 1963) with a distance threshold
187 of 5.5 defined (Supplementary Materials Fig. S1: the largest separation observed from
188 the dendrogram). This waveform similarity analysis highlights five different clusters, as
189 shown in Figure 3b, c. As both the P waves and S waves are used for clustering, the
190 resulting family members should share, to some extend, similarities in position and rupture
191 mechanism (Kagan and Jackson, 1991; Wehling-Benatelli et al., 2013; Cesca et al., 2014;
192 Ellsworth and Bulut, 2018; Cattaneo et al., 1999). However, due to the proximity to
193 the study region of the recording station used in this analysis (VVLD), short S-P time
194 differences are observed for most of the events in the sequence. Therefore, it is important
195 to keep in mind that events occurring in different locations with similar mechanisms might
196 appear strongly related.

197 **Relocation:** We finally estimate the relative location between the detected events using
198 the double-difference algorithm (HypoDD software; Waldhauser (2001)). The differential
199 times of the P phases and S phases between events from the cross-correlation are estimated,
200 with the retention of only the delays that are associated to correlation coefficients >0.6 .
201 We further limit the delays to 0.2 s. After discarding the event pairs that relate less than
202 3 P-wave and 3 S-wave highly correlated differential times (correlation coefficient, ≥ 0.6),
203 the final number of 29859 pairs are kept and used in the relocation process.

204 For each newly detected event, we assume its initial location as the coordinates of the
205 template that reports the highest correlation coefficient related to that event. In addition,
206 we assume the estimated P-wave and S-wave picks obtained from our template matching
207 analysis as the initial catalog information for the relocation. A velocity model for this region
208 proposed by [Bagh et al. \(2007\)](#) is used in the relocation process (Supplementary Materials
209 Table S3). Following previous studies ([Shelly and Hardebeck, 2019](#)), the inversion is per-
210 formed with stronger weights to the initial information related to the P-wave and S-wave
211 picks from the catalog (*i.e.*, from the template matching analysis), while the differential
212 times from the waveform correlations control the final iterations. In the end, 689 of the
213 714 newly detected events are successfully relocated. The temporal and geometric patterns
214 observed in this earthquake sequence are illustrated in Figures 4 and 5, and are further
215 described in the following section.

216 [Figure 3]

217 Results and discussion

218 The time evolution of the detected events is shown in Figure 2. Of the 714 events, 166 are
219 foreshocks (23%). Together with the temporal evolution, Figure 2a shows the spectrogram
220 and the average spectral energy in a frequency band from 5 Hz to 20 Hz. The oscillation
221 of this energy suggests variable noise levels in the study area, with lower noise during the
222 night (Figure 2, shaded areas, for periods from 18:00 to 06:00). This noise variation is
223 related to anthropogenic activity ([Poli et al., 2020b](#)), and it is also observed for the other
224 five receivers. This noise evolution will probably affect our detection performance. For
225 example, it is not clear if the reduced number of events observed prior to the mainshock is
226 real or is a consequence of the higher noise level (Fig. 2b). We thus avoid discussing any
227 issue related to pre-seismic quiescence here. However, with the geometric and clustering

228 information derived above, we can still characterize some of the properties of the newly
229 detected foreshocks and aftershocks, and gain insight into the physical processes that occur
230 at the different stages of the sequence.

231 The results from the combination of waveform clustering and relocation strategies are
232 summarized in Figures 4 and 5. For each cluster, the coefficient of variation (COV) is also
233 estimated from the recurrence time of the events (Kagan and Jackson, 1991; Schoenball
234 and Ellsworth, 2017). The COV indicates the level of the temporal clustering within each
235 group (*i.e.*, how much the occurrence of future earthquakes depends on the occurrence of the
236 past earthquakes): with COV=1 for random seismicity, and COV>1 for strong temporal
237 clustering. The larger the COV, the more the earthquakes are interacting. Thus, it is
238 important to note that events that happen together with a high COV mean that there is
239 an intrinsically related interaction between them.

240 The temporal and spatial densities of the different clusters identified in this sequence
241 are illustrated in Figure 4, where cluster 1 (green solid lines and dots) is mainly composed
242 of foreshocks (161 of 209 events occurred before the mainshock). The events that form this
243 family show the highest waveform similarity (Fig. 3a). In agreement with this waveform
244 property, cluster 1 has high spatial density, with approximately 90% of its activity (193
245 of the 208 events) located within 0.5 km of the mainshock hypocenter (Figs. 4a and 5a).
246 Cluster 1 also shows the highest temporal clustering (COV=4.8; Fig. 4a).

247 The next two families, as cluster 2 (COV=3.0; Figure 4b, blue solid lines and dots)
248 and cluster 3 (COV=2.9; Figure 4c, magenta solid lines and dots), share similar temporal
249 clustering values, but show differences with respect to their spatial densities. While ap-
250 proximately 90% of the events of cluster 2 are within 0.8 km of the hypocenter (136 of 151
251 events; Fig. 4b), cluster 3 has almost 90% of its activity (187 of 211 events) located over
252 a larger volume, as approximately 1.2 km from the mainshock location (Fig. 4c). Cluster
253 4 (Figure 4d, brown solid lines and dots) is characterized by 90% of its activity within 0.6
254 km of the mainshock hypocenter (53 of 59 shocks; Fig. 4d). The seismicity in this cluster

255 is also characterized by high temporal clustering ($\text{COV}=4.2$). Cluster 5 ($\text{COV}=2.2$; Figure
256 4e, red solid lines and dots) is the least temporally clustered, but with the second highest
257 spatial density (after cluster 1), with 90% of its activity in a region 0.5 km from the main-
258 shock hypocenter (66 of 73 events; Fig. 4e). A general spatial pattern of this sequence is
259 the concentration of events close to the mainshock that occurred prior to it (110 foreshocks
260 within 0.3 km) and the subsequent spread over a region >0.3 km during the aftershocks.

261 Figure 5 illustrates the geometric patterns related to each of the clusters, as defined
262 by the relocation process. A remarkable pattern can be seen in Figure 5a: cluster 1 (*i.e.*,
263 foreshocks) shows an antithetical orientation with respect to the assumed fault plane of
264 the main event (Fig. 5a, map view and cross sections). In contrast, clusters 4 and 5 show
265 nearly parallel orientations with respect to the assumed main fault plane (Fig. 5d, e, cross-
266 sections, respectively). We also observe particular behavior for cluster 5, which is the only
267 cluster where the activity is exclusively to the northeast of the mainshock hypocenter and
268 on the footwall (Fig. 5e, map view and cross-sections). The events in cluster 5 follow an
269 orientation that is parallel to the assumed main fault plane dipping angle (Fig. 5e, cross-
270 section). In turn, cluster 3 has an activity that follows the orientation of the fault plane, but
271 that spreads across the whole volume surrounding the fault plane (Fig. 5c, cross-sections).

272 [Figure 4]

273 [Figure 5]

274 The results of the spatio-temporal evolution for the identified clusters suggest complex
275 evolution of the seismicity. Two fault planes are activated during the sequence, with fore-
276 shocks primarily occurring on the antithetic fault plane (Fig. 5a, cross-section), similarly to
277 part of the foreshock activity that was observed for the L'Aquila normal fault earthquake
278 ([Chiaraluce et al., 2011](#)). Relying only on our observations, it is hard to unravel which
279 mechanism(s) might be responsible for the occurrence of the foreshocks, and thus the driv-
280 ing of the main event. For example, there are no exponential or power-law increments

281 of events seen while approaching the main event (Papazachos, 1975; Kagan and Knopoff,
282 1978), which might suggest accelerating aseismic slip (Dodge et al., 1996; Bouchon et al.,
283 2011; Tape et al., 2018). Neither are any spatial patterns seen (*e.g.*, migrations) that might
284 suggest the same mechanism, or might alternatively indicate triggering by stress transfer
285 (Dodge et al., 1996; Ellsworth and Bulut, 2018; Yoon et al., 2019). However, we clearly
286 outline the differences between the foreshocks and aftershocks. In particular, the fore-
287 shocks occur in a more temporal clustered manner, and they are closer to the hypocenter
288 of the main event (Fig. 4a). The compact and highly temporal clustered seismicity indi-
289 cates strong event interactions, and favors stress transfer as the mechanism for foreshock
290 occurrence (COV, Schoenball and Ellsworth, 2017).

291 Analyzing the waveform-based correlation matrix (figure 3a), which is built based only
292 on the similarity of waveforms on the vertical component at the closest station, we are
293 able to distinguish approximately 60 pairs with correlation coefficients larger than 0.95.
294 However, given the fact that most of the events in the sequence have significantly small
295 magnitudes (70% of the events have magnitudes lower than 0.5, figure 2c) and that the
296 frequency range used in the analysis is limited from 5 to 20 Hz, we consider that the
297 available information does not allow us to properly conclude anything about the existance
298 of repeaters in this earthquake sequence (Uchida, 2019; Uchida and Bürgmann, 2019).

299 Interestingly, the aftershock clusters also show different spatio-temporal behaviors be-
300 tween each other (Figs. 5b-e, 4b-e). The observed differences might be explained by different
301 physical processes driving the aftershock occurrence. For example, the events in clusters
302 2 and 3 (Fig. 5b,c) spread in a volume around the fault. This spatial pattern is likely
303 to result from stress redistribution, volumetric damage, and relaxation processes after the
304 mainshock (Trugman et al., 2020). In contrast, clusters 4 and 5 follow the orientation of
305 the main fault in a more compact volume around it (Fig. 5d,e), and their activity decays
306 in a rapid manner (Fig. 4). This behavior might suggest that these latter clusters result
307 from stress increments induced by the mainshock afterslip that occurs near the fault plane

308 region in the few hours or days after the main event (Stein and Lisowski, 1983; Shen et al.,
309 1994). These particular features from clusters 4 and 5 might support the alternative model
310 proposed by ? where the afterslip from the mainshock might be the triggering mechanism
311 of the aftershocks off of the main fault.

312 It is important to point out a particular feature exhibited by cluster 3. Looking at the
313 relative small amplitude of the stacked waveform estimated for cluster 3 (figure 3c) and
314 the resulting relocation of events (figure 5c), we consider that cluster 3 is composed of all
315 the events that share a strong dissimilarity to the remaining events of the sequence. As
316 it was mentioned before, we use the dissimilarity between the waveforms recorded at the
317 closest station to the study region to infer the five different clusters. Therefore, while most
318 of the events show short S-P time differences, these events might be occurring in different
319 locations with similar mechanisms, which is exactly the case of the events from cluster 3.

320 The geometry of the subfaults that were activated during this sequence are not known
321 (except from the main Liri fault). In addition, the focal mechanisms of most of the earth-
322 quakes in the sequence can not be determined due to their small size, noise levels and
323 limited azimuthal coverage of the regional network. The slip distribution of the mainshock
324 and other subevents have not been previously studied. Therefore, the available limited
325 information does not allow to perform a proper Coulomb stress analysis of this sequence
326 (Toda et al., 2011).

327 As in previous studies (McMahon et al., 2017; Savage et al., 2017; McMahon et al., 2019),
328 we can see that this detailed analysis of seismic data reveals a complex and imbricated
329 earthquake sequence, for which the mainshock initiation is unlikely to result from only the
330 evolution of physical properties (*e.g.*, stress, friction) on the main fault plane. Indeed the
331 sequence begins through an interaction between the antithetic and main faults during the
332 foreshock-mainshock sequences, similar to that observed for other events (Chiaraluce et al.,
333 2011; McMahon et al., 2019). In normal faults, this behavior can be related to preseismic
334 processes in the dilation wedge located in the hanging wall (Doglioni et al., 2011). The

complexity of the sequence might also emerge from fluid involvement, which is known to have a significant role in the control of seismicity and its 'style' in the central Apennines (Antonioli et al., 2005; Poli et al., 2020a). The stress perturbations in the antithetic fault might have modified the local pore pressures, with fluid migration into the main fault, which would favor the occurrence of the main event (Doglioni et al., 2011).

Conclusion

By using a combination of high-resolution detection methods, precise relocation (*e.g.*, Gibbons and Ringdal, 2006; Waldhauser, 2001) and waveform clustering, we have unveiled the complexity of the sequences associated with the 2019 (M_w 4.4) Balsorano earthquake. We detect 714 events that comprise this sequence. These events are classified into five different seismic clusters. The differences between these clusters are highlighted by their distinct spatio-temporal properties that are unveiled by the waveform-based clustering analysis (Kagan and Jackson, 1991; Wehling-Benatelli et al., 2013; Cesca et al., 2014; Ellsworth and Bulut, 2018), and by their relative source locations (Waldhauser, 2001).

Our results highlight different behaviors between foreshocks and aftershocks. For example, foreshocks occur in a compact region near the mainshock hypocenter, and show high temporal clustering (Fig. 4a). The lack of repeating events (*i.e.*, highly correlated events with correlation coefficient >0.9), strong temporal clustering, and inter-event proximity might indicate that stress transfer triggering has the main role in driving the occurrence of the foreshocks (Dodge et al., 1996). Nevertheless, there are no observations that can exclude aseismic slip. The foreshock activity mainly take place in an antithetic fault (Fig. 5a), which suggests that the initiation processes do not only occur on one fault plane, but involve larger volumes (Savage et al., 2017). This precursory antithetic activation has been observed in other normal fault events (Chiaraluce et al., 2011) and it can be expected in some gravity-driven normal fault models (Doglioni et al., 2011).

360 Furthermore, our analysis shows diversity for the aftershocks behavior. Indeed, four
361 different clusters comprise the aftershock sequences. Two of these four are spread in a
362 volume around the main fault (Fig. 5b,c), and might result from stress redistribution after
363 the mainshock (*e.g.*, caused by volumetric damage and the relaxation processes; [Trugman](#)
364 [et al. \(2020\)](#)). Given the rapid temporal decay of their activity and their compactness
365 and spatial orientation, the remaining two clusters appear to be driven by rapid stress
366 increments induced by the mainshock and afterslip that occur near the fault plane in the
367 few days after the mainshock ([Stein and Lisowski, 1983](#); [Shen et al., 1994](#)).

368 In summary, this study of foreshocks and aftershocks highlights that simple preparation
369 models with evolution of stress and friction on a single fault plane are not suited to precisely
370 explain the evolution of the seismicity we observe here for a real fault. A relatively large
371 volume appears to be involved in the earthquake initiation, over a short time scale (~ 1 day).
372 We further highlight how the full range of aftershocks is likely to be an ensemble average
373 view of different processes, which will include afterslip, volumetric damage, and relaxation.
374 Continuing to provide detailed information about foreshocks and their relationships to the
375 mainshock and aftershocks also for relatively small events can help us to develop new and
376 more realistic models that can provide better fitting of seismological observations and shed
377 new light on the initiation of earthquakes in real faults.

378 Data and resources

379 The continuous seismic data used in this study are available at the Istituto Nazionale di Ge-
380 ofisica e Vulcanologia (INGV) seismological data center (http://cnt.rm.ingv.it/webservices_and_software/;
381 last accessed, March 2020) and were downloaded using obspyDMT (<https://github.com/kasra-hosseini/obspyDMT>, [Hosseini and Sigloch \(2017\)](#)). The fast matched filter ([Baucé et al., 2017](#)) used in this study can be found at https://github.com/beridel/fast_matched_filter.
384 Some plots were made using the Generic Mapping Tools version 4.5.14 (www.soest.hawaii.edu/gmt;

385 Wessel and Smith (1998)). The event clustering was performed using Scikit-learn (<https://scikit-learn.org/stable/>; Pedregosa et al. (2011))

387 Acknowledgments

388 This research received funding from the European Research Council (ERC) under the Euro-
389 pean Union Horizon 2020 Research and Innovation Programme (grant agreement 802777-
390 MONIAULTS). Computations were performed using the Univerty of Grenoble Alpes
391 (UGA) High-Performance Computing infrastructures CIMENT
392 (<https://ciment.univ-grenoble-alpes.fr>).

393 References

- 394 Abercrombie, R. E. and Mori, J. (1996). Occurrence patterns of foreshocks to large earth-
395 quakes in the western united states. *Nature*, 381(6580):303–307.
- 396 Antonioli, A., Piccinini, D., Chiaraluce, L., and Cocco, M. (2005). Fluid flow and seis-
397 micity pattern: Evidence from the 1997 umbria-marche (central italy) seismic sequence.
398 *Geophysical Research Letters*, 32(10).
- 399 Bagh, S., Chiaraluce, L., De Gori, P., Moretti, M., Govoni, A., Chiarabba, C., Di Bar-
400 tolomeo, P., and Romanelli, M. (2007). Background seismicity in the central apennines
401 of italy: The abruzzo region case study. *Tectonophysics*, 444(1-4):80–92.
- 402 Beaucé, E., Frank, W. B., and Romanenko, A. (2017). Fast matched filter (fmf): An
403 efficient seismic matched-filter search for both cpu and gpu architectures. *Seismological*
404 *Research Letters*, 89(1):165.
- 405 Bouchon, M., Durand, V., Marsan, D., Karabulut, H., and Schmittbuhl, J. (2013). The long
406 precursory phase of most large interplate earthquakes. *Nature geoscience*, 6(4):299–302.

- 407 Bouchon, M., Karabulut, H., Aktar, M., Özalaybey, S., Schmittbuhl, J., and Bouin, M.-P.
408 (2011). Extended nucleation of the 1999 mw 7.6 izmit earthquake. *science*, 331(6019):877–
409 880.
- 410 Brune, J. N. (1979). Implications of earthquake triggering and rupture propagation for
411 earthquake prediction based on premonitory phenomena. *Journal of Geophysical Re-*
412 *search: Solid Earth*, 84(B5):2195–2198.
- 413 Cattaneo, M., Augliera, P., Spallarossa, D., and Lanza, V. (1999). A waveform similarity
414 approach to investigate seismicity patterns. *Natural hazards*, 19(2-3):123–138.
- 415 Cesca, S., Sen, A. T., and Dahm, T. (2014). Seismicity monitoring by cluster analysis of
416 moment tensors. *Geophysical Journal International*, 196(3):1813–1826.
- 417 Chen, X. and Shearer, P. M. (2013). California foreshock sequences suggest aseismic trig-
418 gering process. *Geophysical Research Letters*, 40(11):2602–2607.
- 419 Chiaraluce, L., Valoroso, L., Piccinini, D., Di Stefano, R., and De Gori, P. (2011). The
420 anatomy of the 2009 l'aquila normal fault system (central italy) imaged by high resolu-
421 tion foreshock and aftershock locations. *Journal of Geophysical Research: Solid Earth*,
422 116(B12).
- 423 D'agostino, N., Giuliani, R., Mattone, M., and Bonci, L. (2001). Active crustal extension in
424 the central apennines (italy) inferred from gps measurements in the interval 1994–1999.
425 *Geophysical Research Letters*, 28(10):2121–2124.
- 426 De Santis, A., Marchetti, D., Pavón-Carrasco, F. J., Cianchini, G., Perrone, L., Abbattista,
427 C., Alfonsi, L., Amoruso, L., Campuzano, S. A., Carbone, M., et al. (2019). Precursory
428 worldwide signatures of earthquake occurrences on swarm satellite data. *Scientific reports*,
429 9(1):1–13.

- 430 Dieterich, J. (1994). A constitutive law for rate of earthquake production and its application
431 to earthquake clustering. *Journal of Geophysical Research: Solid Earth*, 99(B2):2601–
432 2618.
- 433 Dieterich, J. H. (1992). Earthquake nucleation on faults with rate-and state-dependent
434 strength. *Tectonophysics*, 211(1-4):115–134.
- 435 Dodge, D. A., Beroza, G. C., and Ellsworth, W. (1996). Detailed observations of califor-
436 nia foreshock sequences: Implications for the earthquake initiation process. *Journal of*
437 *Geophysical Research: Solid Earth*, 101(B10):22371–22392.
- 438 Doglioni, C., Barba, S., Carminati, E., and Riguzzi, F. (2011). Role of the brittle–ductile
439 transition on fault activation. *Physics of the Earth and Planetary Interiors*, 184(3-4):160–
440 171.
- 441 Dublanchet, P. (2018). The dynamics of earthquake precursors controlled by effective fric-
442 tion. *Geophysical Journal International*, 212(2):853–871.
- 443 Eftaxias, K., Kopanas, J., Bogris, N., KAPIRIS, P., ANTONOPOULOS, G., and VAROT-
444 SOS, P. (2000). Detection of electromagnetic earthquake precursory signals in greece.
445 *Proceedings of the Japan Academy, Series B*, 76(4):45–50.
- 446 Ellsworth, W. L. and Beroza, G. C. (1995). Seismic evidence for an earthquake nucleation
447 phase. *Science*, 268(5212):851–855.
- 448 Ellsworth, W. L. and Bulut, F. (2018). Nucleation of the 1999 izmit earthquake by a
449 triggered cascade of foreshocks. *Nature Geoscience*, 11(7):531–535.
- 450 Falcucci, E., Gori, S., Galadini, F., Fubelli, G., Moro, M., and Saroli, M. (2016). Active
451 faults in the epicentral and mesoseismal ml 6.0 24, 2016 amatrice earthquake region,
452 central italy. methodological and seismotectonic issues. *Annals of geophysics*, 59.

- 453 Felzer, K. R., Abercrombie, R. E., and Ekstrom, G. (2004). A common origin for af-
454 tershocks, foreshocks, and multiplets. *Bulletin of the Seismological Society of America*,
455 94(1):88–98.
- 456 Gibbons, S. J. and Ringdal, F. (2006). The detection of low magnitude seismic events using
457 array-based waveform correlation. *Geophysical Journal International*, 165(1):149–166.
- 458 Goebel, T., Becker, T., Schorlemmer, D., Stanchits, S., Sammis, C., Rybacki, E., and
459 Dresen, G. (2012). Identifying fault heterogeneity through mapping spatial anomalies in
460 acoustic emission statistics. *Journal of Geophysical Research: Solid Earth*, 117(B3).
- 461 Hosseini, K. and Sigloch, K. (2017). Obspydmt: a python toolbox for retrieving and pro-
462 cessing large seismological data sets. *Solid Earth*, (5):1047–1070.
- 463 Hunstad, I. and England, P. (1999). An upper bound on the rate of strain in the central
464 apennines, italy, from triangulation measurements between 1869 and 1963. *Earth and*
465 *Planetary Science Letters*, 169(3-4):261–267.
- 466 Jones, L. M. and Molnar, P. (1979). Some characteristics of foreshocks and their pos-
467 sible relationship to earthquake prediction and premonitory slip on faults. *Journal of*
468 *Geophysical Research: Solid Earth*, 84(B7):3596–3608.
- 469 Jones, L. M. (1985). Foreshocks and time-dependent earthquake hazard assessment in
470 southern california. *Bulletin of the Seismological Society of America*, 75(6):1669–1679.
- 471 Kagan, Y. and Jackson, D. D. (1991). Long-term earthquake clustering. *Geophysical Journal*
472 *International*, 104(1):117–133.
- 473 Kagan, Y. and Knopoff, L. (1978). Statistical study of the occurrence of shallow earth-
474 quakes. *Geophysical Journal International*, 55(1):67–86.

- 475 Kato, A., Obara, K., Igarashi, T., Tsuruoka, H., Nakagawa, S., and Hirata, N. (2012).
476 Propagation of slow slip leading up to the 2011 mw 9.0 tohoku-oki earthquake. *Science*,
477 335(6069):705–708.
- 478 Liu, Y. and Rice, J. R. (2005). Aseismic slip transients emerge spontaneously in three-
479 dimensional rate and state modeling of subduction earthquake sequences. *Journal of*
480 *Geophysical Research: Solid Earth*, 110(B8).
- 481 Malin, P. E., Bohnhoff, M., Blümle, F., Dresen, G., Martínez-Garzón, P., Nurlu, M., Ceken,
482 U., Kadirioglu, F. T., Kartal, R. F., Kilic, T., et al. (2018). Microearthquakes preceding
483 a m4. 2 earthquake offshore istanbul. *Scientific reports*, 8(1):1–11.
- 484 Marone, C. (1998). The effect of loading rate on static friction and the rate of fault healing
485 during the earthquake cycle. *Nature*, 391(6662):69–72.
- 486 McLaskey, G. C. (2019). Earthquake initiation from laboratory observations and implica-
487 tions for foreshocks. *Journal of Geophysical Research: Solid Earth*.
- 488 McMahon, N. D., Aster, R. C., Yeck, W. L., McNamara, D. E., and Benz, H. M. (2017).
489 Spatiotemporal evolution of the 2011 prague, oklahoma, aftershock sequence revealed
490 using subspace detection and relocation. *Geophysical Research Letters*, 44(14):7149–7158.
- 491 McMahon, N. D., Yeck, W. L., Stickney, M. C., Aster, R. C., Martens, H. R., and Benz,
492 H. M. (2019). Spatiotemporal analysis of the foreshock–mainshock–aftershock sequence
493 of the 6 july 2017 m w 5.8 lincoln, montana, earthquake. *Seismological Research Letters*,
494 90(1):131–139.
- 495 Mignan, A. (2014). The debate on the prognostic value of earthquake foreshocks: A meta-
496 analysis. *Scientific reports*, 4:4099.
- 497 Mogi, K. (1963). Some discussions on aftershocks, foreshocks and earthquake swarms:
498 the fracture of a semi-infinite body caused by an inner stress origin and its relation to

- 499 the earthquake phenomena (third paper). *Bulletin of the Earthquake Research Institute*,
500 *University of Tokyo*, 41(3):615–658.
- 501 Molchanov, O., Hayakawa, M., Oudoh, T., and Kawai, E. (1998). Precursory effects in the
502 subionospheric vlf signals for the kobe earthquake. *Physics of the Earth and Planetary*
503 *Interiors*, 105(3-4):239–248.
- 504 Papazachos, B. (1975). Foreshocks and earthquake prediction. *Tectonophysics*, 28(4):213–
505 226.
- 506 Pedregosa, F., Varoquaux, G., Gramfort, A., Michel, V., Thirion, B., Grisel, O., Blondel,
507 M., Prettenhofer, P., Weiss, R., Dubourg, V., Vanderplas, J., Passos, A., Cournapeau,
508 D., Brucher, M., Perrot, M., and Duchesnay, E. (2011). Scikit-learn: Machine learning
509 in Python. *Journal of Machine Learning Research*, 12:2825–2830.
- 510 Poli, P., Marguin, V., Wang, Q., Dagostino, N., and Johnson, P. (2020a). Seasonal and co-
511 seismic velocity variation in the region of laquila from single station measurements and
512 implications for crustal rheology. *Journal of Geophysical Research: Solid Earth*, page
513 e2019JB019316.
- 514 Poli, P., Soaga, J., Molinari, I., Cascone, V., and Boschi, L. (2020b). The 2020 coronavirus
515 lockdown and seismic monitoring of anthropic activities in northern italy. *Sci Rep*, 10:–.
- 516 Reasenberg, P. A. (1999). Foreshock occurrence before large earthquakes. *Journal of*
517 *Geophysical Research: Solid Earth*, 104(B3):4755–4768.
- 518 Renard, F., McBeck, J., Kandula, N., Cordonnier, B., Meakin, P., and Ben-Zion, Y. (2019).
519 Volumetric and shear processes in crystalline rock approaching faulting. *Proceedings of*
520 *the National Academy of Sciences*, 116(33):16234–16239.
- 521 Rikitake, T. (1975). Earthquake precursors. *Bulletin of the Seismological Society of Amer-*
522 *ica*, 65(5):1133–1162.

- 523 Roberts, G. P. and Michetti, A. M. (2004). Spatial and temporal variations in growth rates
524 along active normal fault systems: an example from the lazio–abruzzo apennines, central
525 italy. *Journal of Structural Geology*, 26(2):339–376.
- 526 Rubin, A. M. and Ampuero, J.-P. (2005). Earthquake nucleation on (aging) rate and state
527 faults. *Journal of Geophysical Research: Solid Earth*, 110(B11).
- 528 Ruiz, S., Aden-Antoniow, F., Baez, J., Otarola, C., Potin, B., del Campo, F., Poli, P.,
529 Flores, C., Satriano, C., Leyton, F., et al. (2017). Nucleation phase and dynamic inversion
530 of the mw 6.9 valparaíso 2017 earthquake in central chile. *Geophysical Research Letters*,
531 44(20):10–290.
- 532 Ruiz, S., Metois, M., Fuenzalida, A., Ruiz, J., Leyton, F., Grandin, R., Vigny, C.,
533 Madariaga, R., and Campos, J. (2014a). Intense foreshocks and a slow slip event preceded
534 the 2014 iquique mw 8.1 earthquake. *Science*, 345(6201):1165–1169.
- 535 Ruiz, S., Metois, M., Fuenzalida, A., Ruiz, J., Leyton, F., Grandin, R., Vigny, C.,
536 Madariaga, R., and Campos, J. (2014b). Intense foreshocks and a slow slip event preceded
537 the 2014 iquique mw 8.1 earthquake. *Science*, 345(6201):1165–1169.
- 538 Savage, H. M., Keranen, K. M., P. Schaff, D., and Dieck, C. (2017). Possible precursory
539 signals in damage zone foreshocks. *Geophysical Research Letters*, 44(11):5411–5417.
- 540 Schoenball, M. and Ellsworth, W. L. (2017). A systematic assessment of the spatiotemporal
541 evolution of fault activation through induced seismicity in oklahoma and southern kansas.
542 *Journal of Geophysical Research: Solid Earth*, 122(12):10–189.
- 543 Schurr, B., Asch, G., Hainzl, S., Bedford, J., Hoechner, A., Palo, M., Wang, R., Moreno,
544 M., Bartsch, M., Zhang, Y., et al. (2014). Gradual unlocking of plate boundary controlled
545 initiation of the 2014 iquique earthquake. *Nature*, 512(7514):299–302.

- 546 Shelly, D. R., Beroza, G. C., and Ide, S. (2007). Complex evolution of transient slip de-
547 rived from precise tremor locations in western shikoku, japan. *Geochemistry, Geophysics,*
548 *Geosystems*, 8(10).
- 549 Shelly, D. R. and Hardebeck, J. L. (2019). Illuminating faulting complexity of the 2017
550 yellowstone maple creek earthquake swarm. *Geophysical Research Letters*, 46(5):2544–
551 2552.
- 552 Shen, Z.-K., Jackson, D. D., Feng, Y., Cline, M., Kim, M., Fang, P., and Bock, Y. (1994).
553 Postseismic deformation following the landers earthquake, california, 28 june 1992. *Bul-*
554 *letin of the Seismological Society of America*, 84(3):780–791.
- 555 Singh, R. P., Mehdi, W., Gautam, R., Senthil Kumar, J., Zlotnicki, J., and Kafatos, M.
556 (2010). Precursory signals using satellite and ground data associated with the wenchuan
557 earthquake of 12 may 2008. *International Journal of Remote Sensing*, 31(13):3341–3354.
- 558 Stein, R. S. and Lisowski, M. (1983). The 1979 homestead valley earthquake sequence,
559 califonia: Control of aftershocks and postseismic deformation. *Journal of Geophysical*
560 *Research: Solid Earth*, 88(B8):6477–6490.
- 561 Tape, C., Holtkamp, S., Silwal, V., Hawthorne, J., Kaneko, Y., Ampuero, J. P., Ji, C.,
562 Ruppert, N., Smith, K., and West, M. E. (2018). Earthquake nucleation and fault slip
563 complexity in the lower crust of central alaska. *Nature Geoscience*, 11(7):536–541.
- 564 Toda, S., Stein, R. S., Sevilgen, V., and Lin, J. (2011). Coulomb 3.3 graphic-rich defor-
565 mation and stress-change software for earthquake, tectonic, and volcano research and
566 teachinguser guide. *US Geological Survey open-file report*, 1060(2011):63.
- 567 Uchida, N. (2019). Detection of repeating earthquakes and their application in character-
568 izing slow fault slip. *Progress in Earth and Planetary Science*, 6(1):40.

- 569 Uchida, N. and Bürgmann, R. (2019). Repeating earthquakes. *Annual Review of Earth and*
570 *Planetary Sciences*, 47:305–332.
- 571 Tramutoli, V., Corrado, R., Filizzola, C., Genzano, N., Lisi, M., and Pergola, N. (2015).
572 From visual comparison to robust satellite techniques: 30 years of thermal infrared satel-
573 lite data analyses for the study of earthquake preparation phases. *Bollettino di Geofisica*
574 *Teorica ed Applicata*, 56(2).
- 575 Trugman, D. T., Ross, Z. E., and Johnson, P. A. (2020). Imaging stress and fault-
576 ing complexity through earthquake waveform similarity. *Geophysical Research Letters*,
577 47(1):e2019GL085888.
- 578 Virk, H. and Walia, V. (2001). Helium/radon precursory signals of chamoli earthquake,
579 india. *Radiation measurements*, 34(1-6):379–384.
- 580 Waldhauser, F. (2001). hypodda program to compute double-difference hypocenter loca-
581 tions (hypodd version 1.0-03/2001). *US Geol. Surv. Open File Rep.*, 01, 113.
- 582 Ward Jr, J. H. (1963). Hierarchical grouping to optimize an objective function. *Journal of*
583 *the American statistical association*, 58(301):236–244.
- 584 Wedmore, L., Walker, J. F., Roberts, G. P., Sammonds, P., McCaffrey, K., and Cowie, P.
585 (2017). A 667 year record of coseismic and interseismic coulomb stress changes in central
586 italy reveals the role of fault interaction in controlling irregular earthquake recurrence
587 intervals. *Journal of Geophysical Research: Solid Earth*, 122(7):5691–5711.
- 588 Wehling-Benatelli, S., Becker, D., Bischoff, M., Friederich, W., and Meier, T. (2013). In-
589 dications for different types of brittle failure due to active coal mining using waveform
590 similarities of induced seismic events. *Solid Earth*, 4(2).
- 591 Wessel, P. and Smith, W. H. (1998). New, improved version of generic mapping tools
592 released. *Eos, Transactions American Geophysical Union*, 79(47):579–579.

- 593 Westaway, R. (1992). Seismic moment summation for historical earthquakes in italy: tec-
594 tonic implications. *Journal of Geophysical Research: Solid Earth*, 97(B11):15437–15464.
- 595 Yoon, C. E., Yoshimitsu, N., Ellsworth, W. L., and Beroza, G. C. (2019). Foreshocks and
596 mainshock nucleation of the 1999 m w 7.1 hector mine, california, earthquake. *Journal
597 of Geophysical Research: Solid Earth*, 124(2):1569–1582.
- 598 Zang, A., Christian Wagner, F., Stanchits, S., Dresen, G., Andresen, R., and Haidekker,
599 M. A. (1998). Source analysis of acoustic emissions in aue granite cores under symmetric
600 and asymmetric compressive loads. *Geophysical Journal International*, 135(3):1113–1130.

601 Figure Captions

Figure 1. Regional map of the study area. The yellow square inside the small map inset on the left corresponds to the central region of Italy represented in the larger topographic map. The small map inset on the right represents magnification of the black dashed area around the epicentral location (red star). The color code used in the map view on the right represents the estimated depth of the foreshock and aftershock activity (estimated in this study: 714 events). The yellow circle represents Balsorano city, and the white triangles represent the stations used in this study. The dashed lines in the right inset map represent the directions A-A' (along strike) and B-B' (normal to the strike) illustrated in the cross sections of Figure 5. The solid red line represents the superficial scarp of the Liri fault (scarp taken from [Wedmore et al. \(2017\)](#)).

Figure 2. (a) Spectrogram on VVLD.HHZ. The white line is the median of the energy in the frequency band between 5 Hz and 20 Hz calculated within a 1-h sliding window. Notice the diurnal energy variation. (b) Blue, cumulative events for the same time period of the experiment; orange, recurrence time for the newly detected events. (c) Estimated magnitudes for the newly detected events. A gap in the continuous data at this receiver location is seen for the night of November 8 to 9, 2019. In all pannels, day and night periods are represented by shaded (18:00 to 6:00) and unshaded (6:00 to 18:00) regions.

Figure 3. Illustration of the waveform-based hierarchical clustering output. (a) Pairwise correlation coefficients between the waveforms for the vertical component of station VVLD (Fig. 1) of the 714 detected events. This matrix is used to perform the hierarchical clustering. (b) Cumulative events combined with the results from the hierarchical clustering, according to the color code in the legend. (c) Characteristic normalized waveforms (vertical

component) of the five different clusters revealed in the earthquake sequence. These traces are obtained after stacking all of the individually normalized waveforms belonging to each cluster.

Figure 4. Spatio-temporal evolution of the earthquake sequences with respect to the mainshock origin time and hypocenter. Left column: Temporal density (number of events per hour). The coefficients of variation (COV) from the recurrence times are indicated for each cluster. Center column: Distance in time and space from each event of the sequence with respect to the mainshock location and origin time. The dashed grey line on the left and center column represents the mainshock origin time. Right column: Spatial density (concentration of events per 0.1 km). Dashed black line, where 90% of the seismic activity is concentrated. (a)-(e) Each of the five clusters progressively ordered. The same color code from Figure 3 is used.

Figure 5. Map view (left column), and cross-sections along the strike (middle column) and normal-strike (right column) directions for each of the five clusters identified in the sequence (as indicated). All of the locations are relative to the mainshock hypocenter (41.7746°N 13.6066°E ; 13.94 km depth, black star). In all of the panels, the same color code is used as in Figures 3 and 4 to represent each different cluster. The solid black line represents a fault plane of 1 km^2 with the geometry of the second nodal plane (Supplementary Materials Table S1). The dashed blue line represents the assumed auxiliary nodal plane. The directions A-A' (along strike) and B-B' (normal to the strike) are the same as in Figure 1. Each cluster is represented by a correponding label a) Cluster 1 , b) Cluster 2, c) Cluster 3, d) Cluster 4 and e) Cluster 5. In each panel, the black circles represent the location of the templates belonging to each cluster.

602 Figures

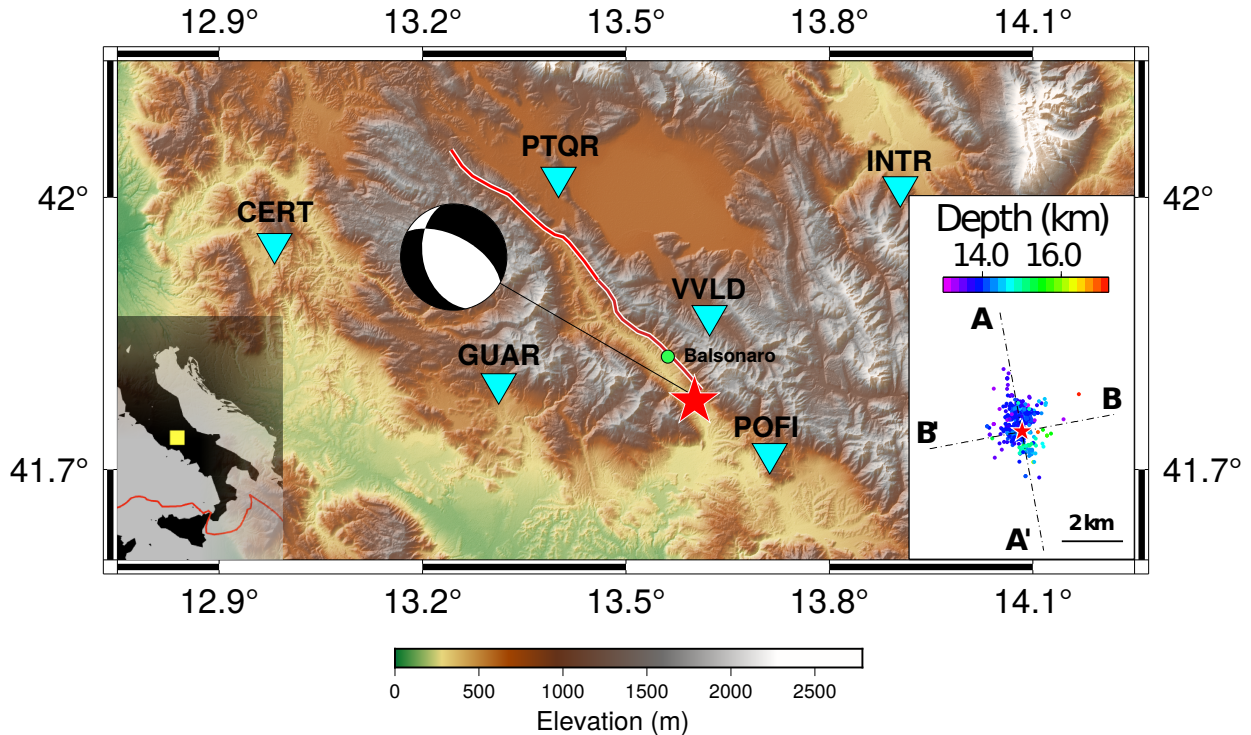


Figure 1: Regional map of the study area. The yellow square inside the small map inset on the left corresponds to the central region of Italy represented in the larger topographic map. The small map inset on the right represents magnification of the black dashed area around the epicentral location (red star). The color code used in the map view on the right represents the estimated depth of the foreshock and aftershock activity (estimated in this study: 714 events). The yellow circle represents Balsorano city, and the white triangles represent the stations used in this study. The dashed lines in the right inset map represent the directions A-A' (along strike) and B-B' (normal to the strike) illustrated in the cross sections of Figure 5. The solid red line represents the superficial scarp of the Liri fault (scarp taken from [Wedmore et al. \(2017\)](#)).

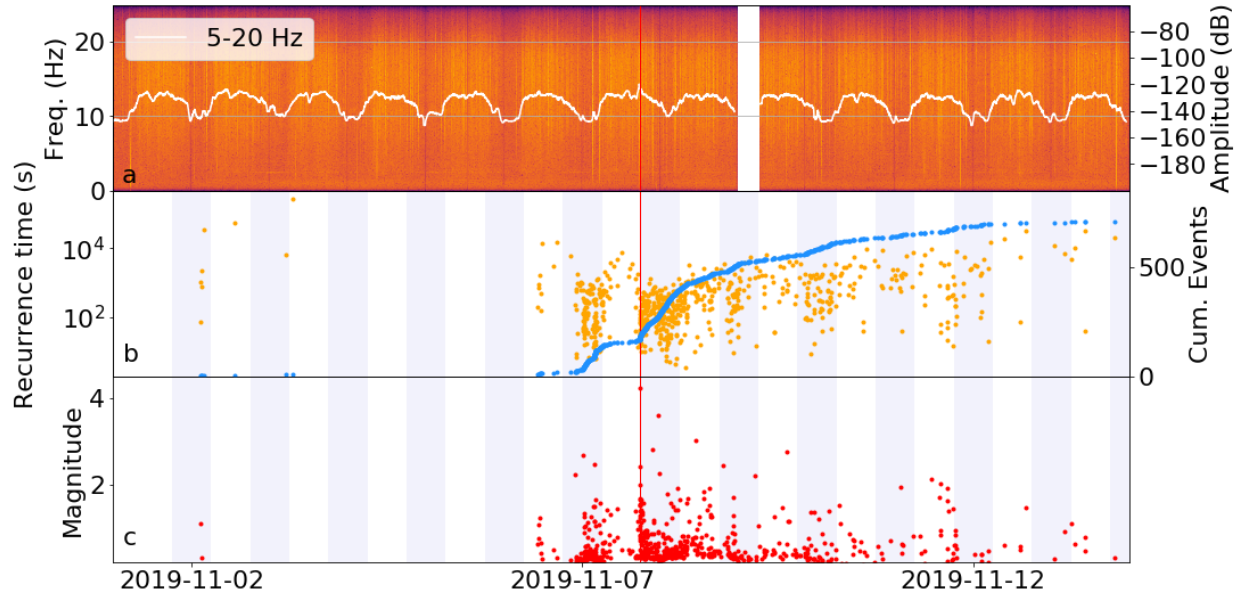


Figure 2: (a) Spectrogram on VVLD.HHZ. The white line is the median of the energy in the frequency band between 5 Hz and 20 Hz calculated within a 1-h sliding window. Notice the diurnal energy variation. (b) Blue, cumulative events for the same time period of the experiment; orange, recurrence time for the newly detected events. (c) Estimated magnitudes for the newly detected events. A gap in the continuous data at this receiver location is seen for the night of November 8 to 9, 2019. In all panels, day and night periods are represented by shaded (18:00 to 6:00) and unshaded (6:00 to 18:00) regions.

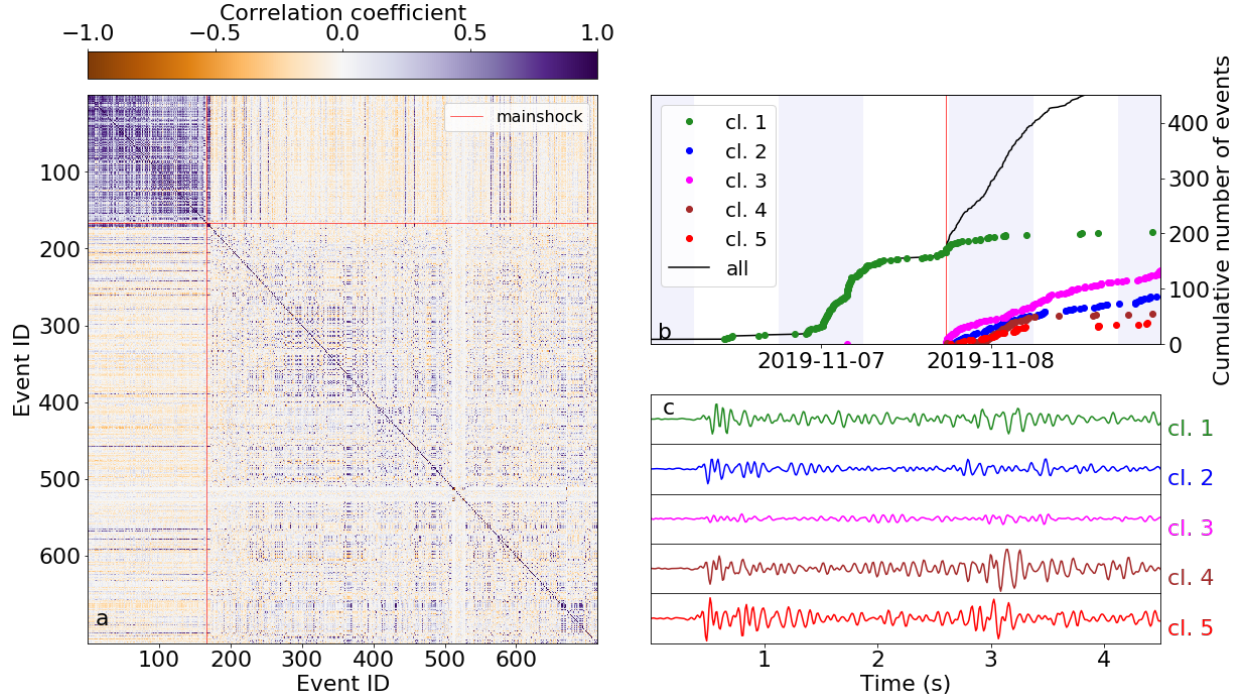


Figure 3: Illustration of the waveform-based hierarchical clustering output. (a) Pairwise correlation coefficients between the waveforms for the vertical component of station VVLD (Fig. 1) of the 714 detected events. This matrix is used to perform the hierarchical clustering. (b) Cumulative events combined with the results from the hierarchical clustering, according to the color code in the legend. (c) Characteristic normalized waveforms (vertical component) of the five different clusters revealed in the earthquake sequence. These traces are obtained after stacking all of the individually normalized waveforms belonging to each cluster.

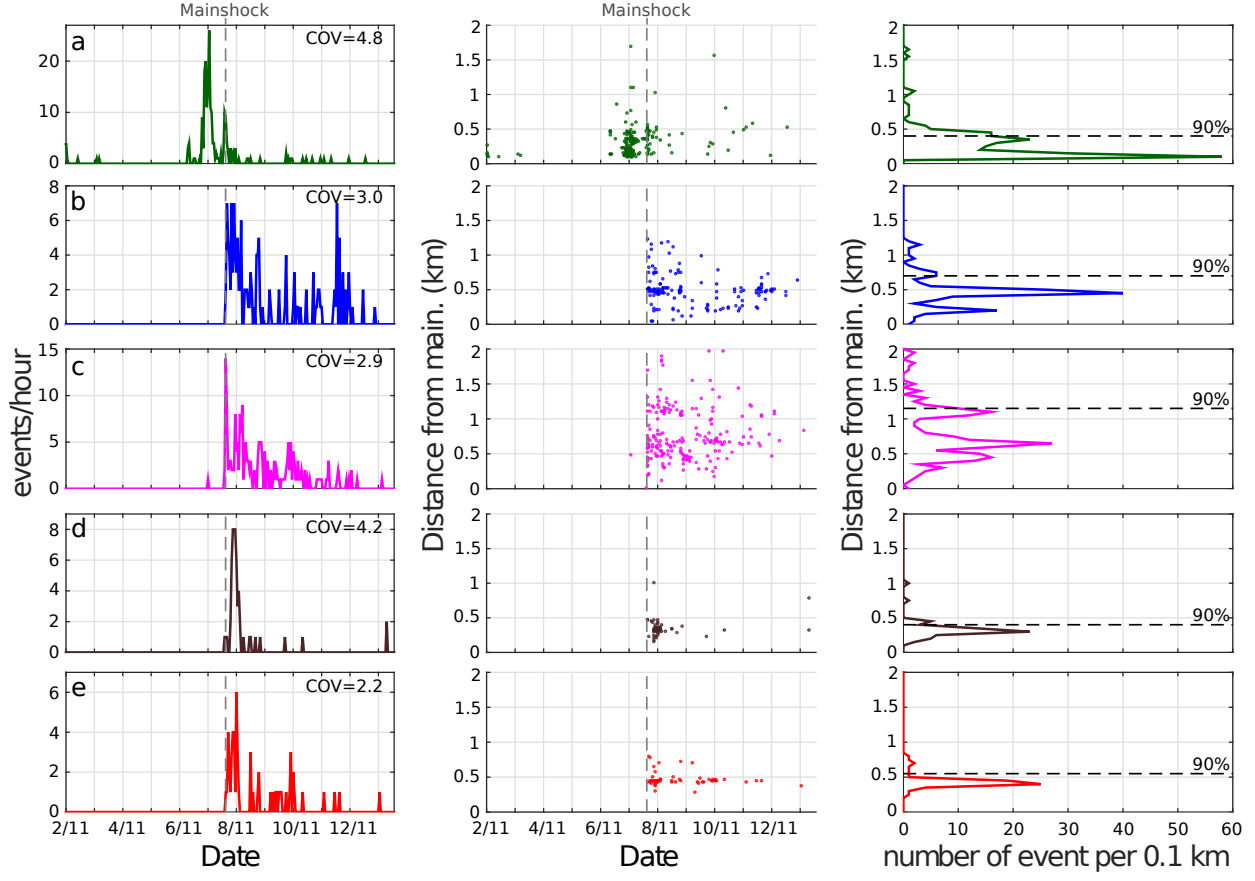


Figure 4: Spatio-temporal evolution of the earthquake sequences with respect to the mainshock origin time and hypocenter. Left column: Temporal density (number of events per hour). The coefficients of variation (COV) from the recurrence times are indicated for each cluster. Center column: Distance in time and space from each event of the sequence with respect to the mainshock location and origin time. The dashed grey line on the left and center column represents the mainshock origin time. Right column: Spatial density (concentration of events per 0.1 km). Dashed black line, where 90% of the seismic activity is concentrated. (a)-(e) Each of the five clusters progressively ordered. The same color code from Figure 3 is used.

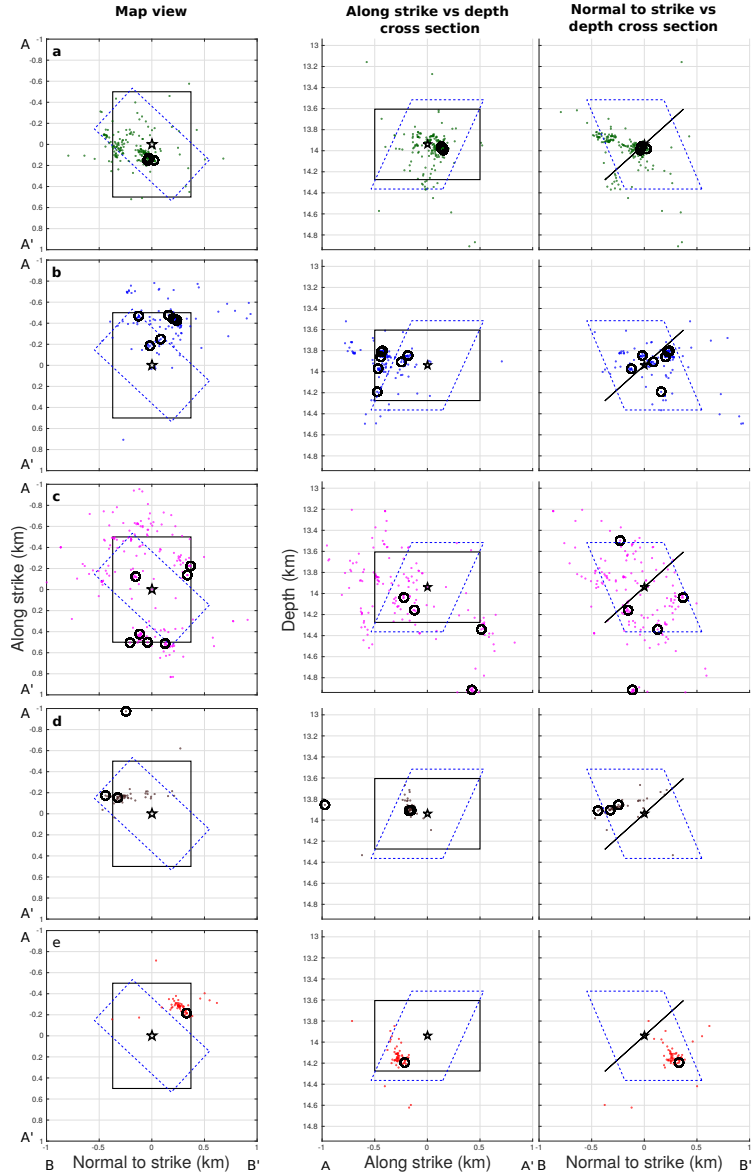


Figure 5: Map view (left column), and cross-sections along the strike (middle column) and normal-strike (right column) directions for each of the five clusters identified in the sequence (as indicated). All of the locations are relative to the mainshock hypocenter (41.7746°N 13.6066°E ; 13.94 km depth, black star). In all of the panels, the same color code is used as in Figures 3 and 4 to represent each different cluster. The solid black line represents a fault plane of 1 km^2 with the geometry of the second nodal plane (Supplementary Materials Table S1). The dashed blue line represents the assumed auxiliary nodal plane. The directions A-A' (along strike) and B-B' (normal to the strike) are the same as in Figure 1. Each cluster is represented by a corresponding label a) Cluster 1 , b) Cluster 2, c) Cluster 3, d) Cluster 4 and e) Cluster 5. In each panel, the black circles represent the location of the templates belonging to each cluster.